Acetaldehyde degradation under UV and visible irradiation using CeO$_2$–TiO$_2$ composite systems: Evaluation of the photocatalytic efficiencies

Mario J. Muñoz-Batista [a], María de los Milagros Ballari [b], Anna Kubacka [a], Alberto E. Cassano [b], Orlando M. Alfano [b],*, Marcos Fernández-García [a],*

[a] Instituto de Catálisis y Petroleoquímica, CSIC, C/Marie Curie 2, 28049 Madrid, Spain
[b] Instituto de Desarrollo Tecnológico para la Industria Química (INTEC), UNL – CONICET, Güemes 3450, 3000 Santa Fe, Argentina

HIGHLIGHTS

- CeO$_2$–TiO$_2$ materials were prepared by a single-pot microemulsion procedure.
- Optimum performance achieved with a 2.5 M% loading of Ce.
- Efficiency parameters demonstrates the improvement of activity with respect to titania.
- CeO$_2$–TiO$_2$ materials appears as an optimum choice for solar light profiting.

GRAPHICAL ABSTRACT
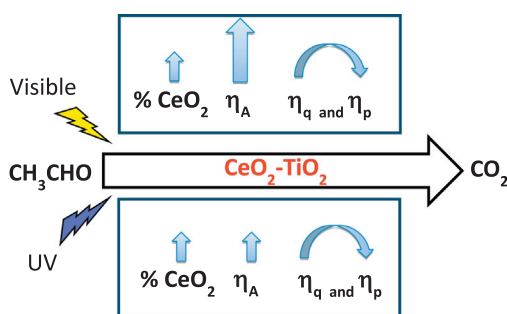
ABSTRACT

The photocatalytic activity under UV and visible irradiation of a series of CeO$_2$–TiO$_2$ composite materials prepared by microemulsion and subsequently calcined at 500 °C was evaluated using acetaldehyde as a model pollutant. The activities of three composite catalysts containing 2.5, 5 and 25 M% of ceria, as well as a nano-titania reference are compared by means of efficiency parameters; the quantum (or true) efficiency, as well as the photonic (or apparent) efficiency were evaluated. To this end, the lamp emission properties, as well as the radiation field interaction with the catalyst inside the reactor were modeled and numerically calculated. For the evaluation of the radiation absorbed by the catalysts, the optical properties of the materials were measured and a radiative transfer model that considers all potential optical events was built up. The stability of the systems under reaction conditions was also studied. Overall, the results evidence that the composite containing 2.5 Ce mol% outperforms titania by a factor of at least 2, irrespective of the illumination source used in the experiment. This shows the potential of the CeO$_2$–TiO$_2$ composites, a highly active and stable system, for sunlight optimum profiting.

© 2014 Elsevier B.V. All rights reserved.

1. Introduction

Heterogeneous photocatalysis is an Advanced Oxidation Process using nanocrystalline semiconductors useful in both the degradation of organic and biological pollutants. It is essentially based on the excellent performance and stability of titania, the most prominent photocatalytic material. Titania is used in the mineralization of numerous pollutants or the inactivation of dangerous microorganisms, typically carried out under mild conditions, e.g. room temperature and atmospheric pressure, and using oxygen (air) as

---

Nomenclature

A_{BET}	BET surface area, $m^2\,g^{-1}$
C	concentration, $g\,m^{-3}$
$e^{a,s}$	local superficial rate of photon absorption, Einstein $cm^{-2}\,s^{-1}$
I	radiation intensity, Einstein $cm^{-2}\,s^{-1}\,sr^{-1}$
m	mass of catalyst, g
$\underline{n}_G$	outwardly directed (to the catalytic film) unit normal vector, dimensionless
P	emission power, W
q	local net radiation flux, Einstein $cm^{-2}\,s^{-1}$
$\underline{q}$	local radiation flux vector, Einstein $cm^{-2}\,s^{-1}$
$\overline{Q}$	volumetric flow rate of the Ω stream fed, $m^3\,s^{-1}$
r	superficial reaction rate, $mol\,m^{-2}\,s^{-1}$
R_L	lamp radius, cm
x, y, z	cartesian coordinate, cm
Z_L	lamp length, cm

Greek letters

φ, θ	spherical coordinate, rad
λ	wavelength, nm
η_I	radiation incidence efficiency, %
η_A	radiation absorption efficiency, %
η_q	quantum (or true) efficiency, %

η_p	photonic (or apparent) efficiency, %
Ω	solid angle, sr
$\underline{\Omega}$	unit vector in the direction of radiation propagation, dimensionless

Subscripts

a	relative to acrylic
Ac	relative to acetaldehyde
gl	relative to glass
i	relative to i-th medium
in	relative to the inlet stream of the reactor
L	relative to lamp
Lm	relative to the surface lamp
max	maximum limiting value
min	minimum limiting value
out	relative to the outlet stream of the reactor
s	relative to the sample film
λ	dependence on wavelength

Special symbols

$\langle * \rangle$	average value

oxidant agent. Among titania polymorphs, anatase appears as the most active single phase [1–4]. However, the main limitation of anatase comes from its relatively wide band gap energy, ca. 3.0–3.4 eV, which demands UV radiation for triggering photo-redox reactions. Because UV radiation only accounts for ca. 3–5% of the solar spectrum, photocatalytic efficiency of pure titania-based photocatalysts under sunlight is limited. The use of the visible part of the solar spectrum, ca. 45%, has forced to implement several strategies aiming to profit from the complete solar spectrum and, particularly, the visible region. Among the mentioned strategies, the use of visible-light-sensitize phases in intimate contact with TiO₂ has shown to be particularly successful [1–4]. Specifically, the use of ceria as a solid-state sensitizer has demonstrated a high potential in the photoelimination of contaminants [5–14]. Ceria can extent absorption capabilities of the catalyst up to ca. 550 nm (e.g. around 175 nm above the point where titania absorption becomes negligible) and has photocatalytic activity by itself [15–18].

However, comparison of photocatalysts employing efficiency parameters has been rarely reported in the cases above mentioned. This can limit the generalization of the presented results and thus complicate the interpretation of the effectiveness of the CeO₂–TiO₂ composite materials. The calculation of efficiency parameters involves the measurement and modeling of the reached radiation at the material surface and the fraction effectively absorbed by the photocatalytic initiation step(s). Such task typically involves, in first place, the measurement and modeling of the light source emission properties [19–23] and, subsequently, the absorption capability of the photocatalysts. The latter requires the calculation of the local superficial rate of photon absorption, $e^{a,s}$. This has been carried out previously in a series of contributions with different reactor configurations [24–26].

In this contribution we aim to analyze the photo-oxidation of acetaldehyde as a model pollutant [27] using recently developed CeO₂–TiO₂ composite materials [13,14,26]. UV and visible light illumination conditions are considered. Among the possible Ce–Ti molar ratios, we selected specific samples showing optimum activity under both UV and visible illumination conditions [13,14,26].

These samples were also compared with another Ce–Ti composite sample displaying poor activity, as well as with the appropriate single phase titania reference material. Moreover, the performance of these samples is compared using two parameters: (i) the quantum (or true) efficiency, which relates the moles of degraded pollutant with the moles of the absorbed photons; and (ii) the photonic (or apparent) efficiency, which relates the moles of degraded pollutant with the moles of incident photons [28–32]. The quantitative analysis of the activity evidences that CeO₂–TiO₂ composite system as an useful candidate for optimal profiting of solar light.

2. Experimental

2.1. Catalyst preparation

The catalytic materials were prepared using a microemulsion preparation method using *n*-heptane (Scharlau) as organic media, Triton X-100 (Aldrich) as surfactant and hexanol (Aldrich) as cosurfactant. A TiO₂ reference sample was obtained as a first step using a microemulsion into the aqueous phase and titanium tetraisopropoxide as precursor [13,26]. In all composite samples and the CeO₂ reference, cerium nitrate (Alfa Aesar) was introduced in the aqueous phase of a microemulsion. After 30 min of agitation, a stoichiometric (to obtain the corresponding Ce(III) hydroxide) quantity of tetramethylammonium-hydroxide (TMAH) was introduced from the aqueous phase of a similar microemulsion. For nanocomposite samples, after 5 min, titanium tetraisopropoxide was introduced into the previously resulting microemulsion drop by drop from a mixture with isopropanol (2:3). Water/TiO₂ and water/surfactant molar ratios were 110 and 18 for all samples, respectively [33,34]. The resulting mixture was stirred for 24 h, centrifuged, and the separated solid precursors rinsed with methanol and dried at 110 °C for 12 h. After drying, the solid precursors were subjected to a heating ramp (2 °C min⁻¹) up to 500 °C, maintaining this temperature for 2 h. Samples names are Ti for the TiO₂ reference, and *x*CeTi for the composite ones where x is the molar content of CeO₂ (in relation to a fixed amount of TiO₂ corresponding to 1 mol).

2.2. Characterization

XRD profiles were obtained with a Seifert D-500 diffractometer using Ni-filtered Cu Kα radiation with a 0.02° step and fitted using the Von Dreele approach to the Le Bail method. Particle sizes were measured with XRD using the Williamson-Hall formalism. UV–visible diffuse reflectance spectroscopy experiments were performed with a Shimadzu UV2100 apparatus using, for diffuse experiments, $BaSO_4$ as reference. The optical properties of the immobilized TiO_2–CeO_2 composites on the glass plate were determined as a function of wavelength between 300 and 600 nm in an Optronic OL Series 750 spectroradiometer equipped with an OL 740-70 integrating sphere reflectance attachment. To evaluate the fraction of energy absorbed by the catalytic film the spectral diffuse reflectance and the spectral diffuse transmittance of the coated glass were experimentally determined. The BET surface areas and average pore volume and sizes were measured by nitrogen physisorption (Micromeritics ASAP 2010). Raman spectra of samples were collected with an iHR320 Horiba Jobin-Yvon spectrometer equipped with a He:Ne laser (633 nm).

2.3. Reactor system and experimental conditions

Fig. 1 provides a scheme of the used apparatus to study the photodegradation of acetaldehyde in gas phase. The corresponding amount of catalyst was suspended in 2 mL of ethanol, painted on a borosilicate plate and dried at RT. The reaction chamber was confined between two rectangular acrylic windows (20×9.5 cm^2). Each catalytic plate was exposed to the radiation coming from two sets of seven UV (Philips TL 4W/08 F4T5/BLB) or Visible (General Electric GE F4T5/CW) emitting lamps; each set faced one sample plate side (spectral emission of the lamps are presented at the Supporting Information, Fig. S1). The lamps in each set were arranged with a separation between axes of 2.6 cm, and the distance from them to the reactor center plane was 4.3 cm. Acetaldehyde was used as the pollutant supplied from a cylinder containing 300 ppm of acetaldehyde in nitrogen. The acetaldehyde was mixed with streams of air and water-saturated air to obtain the concentration and relative humidity required (20 ppm and 45% respectively). The flow rates of reactive gases were controlled by online mass-flow controllers (Aalborg). The total flow rate of the
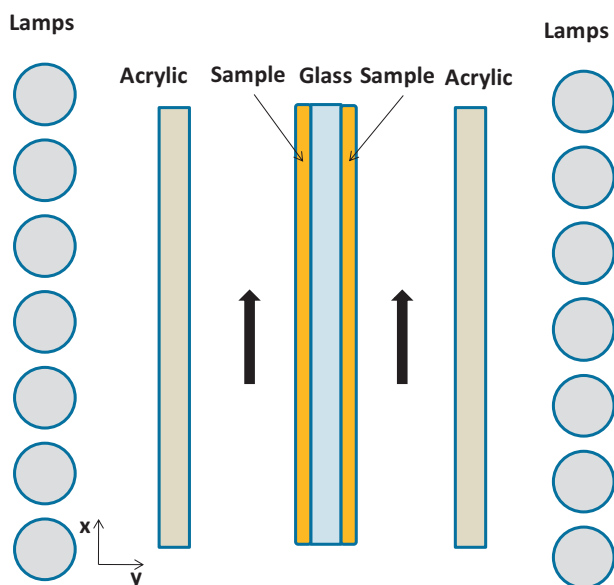
Table 1
Experimental operating conditions.

Operating Conditions	Unit	Value
Flow rate	cm^3 min^{-1}	1000
Temperature	°C	25
Pressure	atm	1
Inlet concentration	ppm	20
Relative humidity	%	45
UV incident irradiance[a]	W cm^{-2}	4.02×10^{-3}
Visible incident irradiance[a]	W cm^{-2}	6.62×10^{-3}

[a] Measured at center of the reactor.

reaction mixture was 1000 mL/min. The temperature and the humidity of the feed stream were measured with an online thermo-hygrometer located before the inlet point of photoreactor. The concentration of the reactants and products was analyzed using offline gas chromatography (Hewlett-Packard 5890 Series II; J&W Scientific INC. DB-1301 column; FID detector) performing a direct injection of the gas sample. Steady state conditions are achieved in relativity short reaction time. Full experimental details are given in Table 1.

3. Radiation model

The local net radiation flux on the catalytic film, q_λ at each position (x,y,z) is defined by Eq. (1) [32].

$$q_\lambda(x,y,z) = \underline{n}_G \cdot \underline{q}_\lambda(x,y,z) = \int_{\Omega_L} I_\lambda(x,y,z,\underline{\Omega})\underline{\Omega} \cdot \underline{n}_G d\Omega \tag{1}$$

where $\underline{n}_G$ is the outwardly directed unit vector normal to the catalytic film and I_λ is the intensity associated to a beam of rays carrying energy of wavelength λ in the direction of the solid angle unit vector $\underline{\Omega}$.

The solution of this equation requires the representation of a three-dimensional light source. According to the coordinate system adopted (Fig. 2) and the photoreactor geometry:

$$\underline{\Omega} \cdot \underline{n}_G = \cos \varphi \sin \theta \tag{2}$$

$$d\Omega = \sin \theta \, d\varphi d\theta \tag{3}$$

The radiation flux on each (lamp set faced) plate side is thus given by Eq. (4).
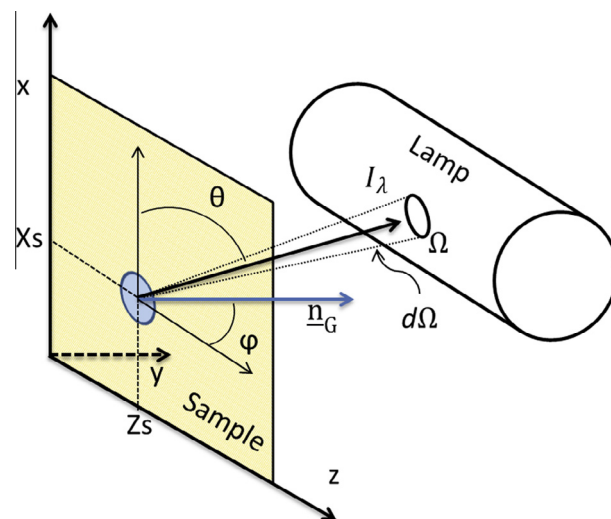

Fig. 1. Scheme of the photocatalytic reactor.

Fig. 2. Coordinate system adopted for the reactor-lamps system.

$$q(x,y,z) = \sum_{L=1}^{L=7}\sum_{\lambda} \int_{\varphi\min,L}^{\varphi\max,L} \int_{\theta\min,L}^{\theta\max,L} I_{\lambda,L}\sin^2\theta\cos\varphi \; d\varphi d\theta \tag{4}$$

The integration limits for the spherical coordinate (φ and θ) can be evaluated from the geometry and dimensions of the system and lamps. A complete description is presented in the Appendix A.

Considering the assumptions of the surface lamp emission model [35], the radiation intensity is calculated by:

$$I_{\lambda,L}(x,y,z,\varphi,\theta) = \begin{cases} 0 & (\varphi,\theta) < (\varphi_{\min,L},\theta_{\min,L}) \\ \frac{P_{\lambda,L}}{2\pi^2 R_L Z_L} & (\varphi_{\min,L},\theta_{\min,L}) < (\varphi,\theta) < (\varphi_{\max,L},\theta_{\max,L}) \\ 0 & (\varphi_{\max,L},\theta_{\max,L}) < (\varphi,\theta) \end{cases} \tag{5}$$

where $P_{\lambda,L}$ is the spectral emission power of the lamp, and R_L and Z_L are the radius and length of the i-th lamp, respectively.

The double integral of Eq. (4) was solved numerically and compared with experimental values obtained with a radiometer. These results are shown in Fig. S2(A) and (B) in the Supporting Information. The differences between experimental data and model predictions were 7% and 10% for UV and visible lamp, respectively.

To obtain the absorbed radiation at each x,y,z point on the sample surface, the so-called local superficial rate of photon absorption, $e^{a,s}$, is computed as indicated by Eq. (6) for right plate and Eq. (7) for left plate. The $a_{i,\lambda}$ symbol denotes the spectral fraction of absorbed incident energy by the i-th medium., $q_{1,\lambda}^+$, $q_{2,\lambda}^-$, $q_{4,\lambda}^-$, $q_{3,\lambda}^+$ are the net radiation fluxes impinging on each side of the plate according to Fig. 3.

$$e_{\lambda,\text{right}}^{a,s}(x,y,z) = a_{s,\lambda}q_{1,\lambda}^+(x,y,z) + a_{s,\lambda}q_{2,\lambda}^-(x,y,z) \tag{6}$$

$$e_{\lambda,\text{left}}^{a,s}(x,y,z) = a_{s,\lambda}q_{4,\lambda}^-(x,y,z) + a_{s,\lambda}q_{3,\lambda}^+(x,y,z) \tag{7}$$

Eqs. (6) and (7) would provide the same value at x,±y,z points for the right or left surface of the sample according to the symmetry of the system (see Figs.1 and 3).

The mathematical expressions to calculate the fraction of absorbed incident energy at the i-th medium is given by Eq. (8).

$$a_{i,\lambda} = 1 - T_{i,\lambda} - R_{i,\lambda} \tag{8}$$

where ($T_{i,\lambda}$) and ($R_{i,\lambda}$) are the spectral diffuse transmittance and reflectance, respectively.

The final expression of $e^{a,s}$ at each s point on the catalytic plate (in the specific case of the right plate; see Fig. 3) is given by Eq. (9). This equation is obtained from a local radiative energy balance in terms of local net radiation fluxes (Fig. 3) using the methodology developed for the case system consisting in parallel glass plates [36]. This approach takes into account multiple reflections, absorptions and transmissions of radiation of the different media. Note that the final equation is expressed only in terms of the fraction of incident energy transmitted, reflected and absorbed by acrylic (a), glass (gl), and sample (s).

$$e_{\lambda}^{a,s}(x,y,z) = q_{\lambda}(x,y,z)a_{a,\lambda}a_{s,\lambda}$$
$$\times \left(1 + \frac{R_{gl,\lambda}T_{s,\lambda} - R_{gl,\lambda}^2 R_{s,\lambda}T_{s,\lambda} + T_{gl,\lambda}T_{s,\lambda} + T_{gl,\lambda}^2 R_{s,\lambda}T_{s,\lambda}}{1 - 2R_{gl,\lambda}R_{s,\lambda} + R_{gl,\lambda}^2 R_{s,\lambda}^2 - T_{gl,\lambda}^2 R_{s,\lambda}^2}\right) \tag{9}$$

In order to evaluate these properties, the diffuse transmittance and reflectance of the glass plate (gl), acrylic (a) and catalyst deposited on the plate (s, gl) were measured as a function of the wavelength within the emission range of the lamps. The diffuse transmittance and reflectance of the catalysts can be obtained using the ray-tracing method according to Eqs. (10) and (11) [32]. The transmittance and reflectance of participative items (a, gl, s) are shown in Fig. 4. Local superficial rate of photon absorption for the samples and the lamp used are presented in Figs. 5 and 6.

$$T_{s,\lambda} = \frac{T_{s,gl,\lambda}T_{gl,\lambda}(-1 + R_{s,gl,\lambda}R_{gl,\lambda})}{R_{gl,\lambda}^2 T_{s,gl,\lambda}^2 - T_{gl,\lambda}^2} \tag{10}$$

$$R_{s,\lambda} = -\frac{-R_{gl,\lambda}T_{s,gl,\lambda}^2 + R_{s,gl,\lambda}T_{gl,\lambda}^2}{R_{gl,\lambda}^2 T_{s,gl,\lambda}^2 - T_{gl,\lambda}^2} \tag{11}$$

4. Results

4.1. Post-reaction characterization

A complete characterization of the samples has been presented in a previous work [13]. Such work demonstrated that the oxide-oxide contact can control photoactivity through the number of hole-related species available at the surface of the composite materials and that such number is, in turn, related to the stabilization of reduced Ce species present at the CeO$_2$–TiO$_2$ interface [13]. In this case we focus on a post-reaction characterization to demonstrate the stability of the samples after acetaldehyde photo-degradation. Table 2 reports the main physico-chemical parameters of the materials synthesized. This result indicates: (i) good correspondence between theoretical and real molar% of samples obtained with TXRF; (ii) small CeO$_2$-type clusters tend to be located into anatase pores; (iii) loose-contacting ceria nanoparticles corresponding to an additional Ce-containing component of the 0.25CeTi catalyst; (iv) good homogeneity of crystal size (ca. 12–15 nm for anatase and 5.0–9.5 nm for fluorite). The XRD patterns used to determinate the primary particle size are presented in Fig. 7. We detect the anatase (JCPDS card 78-2486, corresponding to the *I*41/*and* space group) and fluorite (JCPDS card 87-0792, corresponding to the *Fm3m* space group) structures for, the TiO$_2$ and
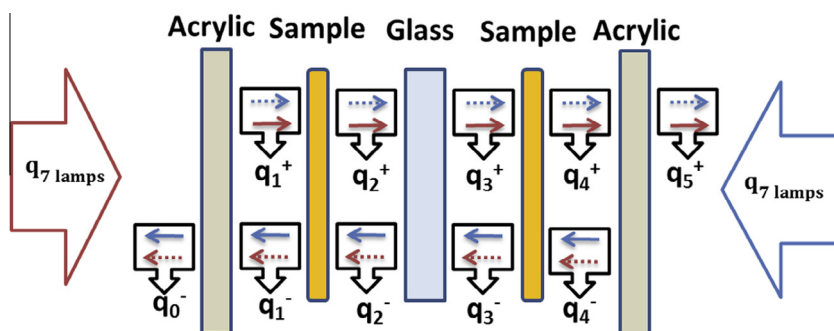

Fig. 3. Schematic representation of the radiation balance. Solid arrow: transmitted radiation flux; dotted arrow: reflected radiation flux.
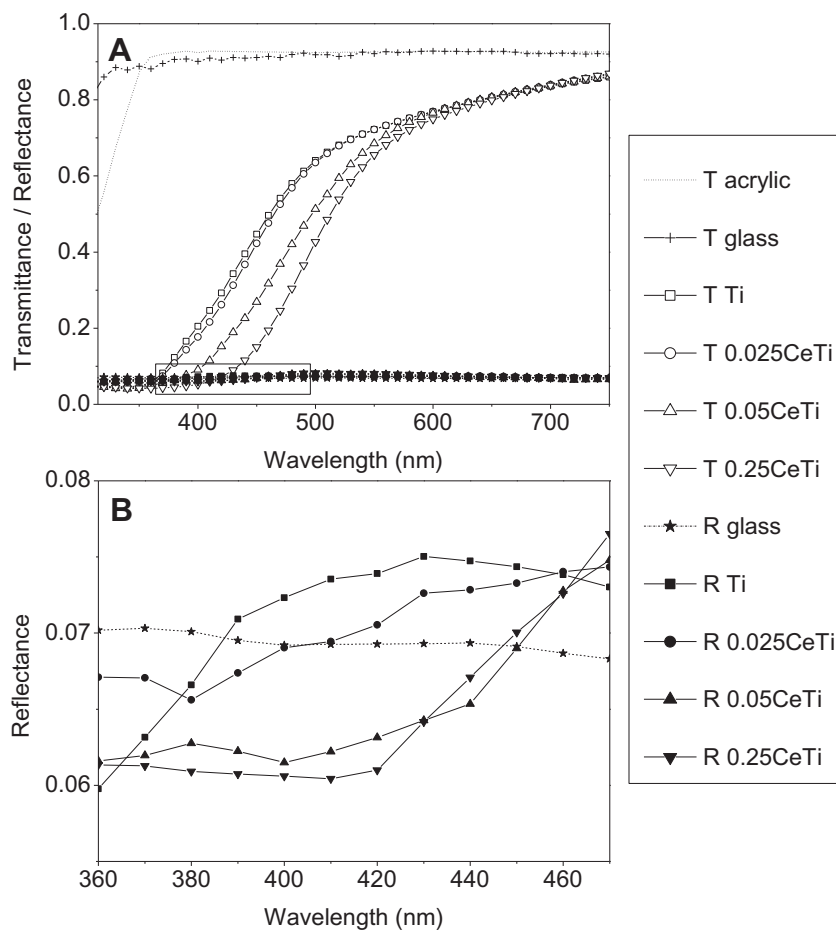
Fig. 4. (A) Transmittance (T) and reflectance (R) experimental values of the borosilicate plate, acrylic and samples. (B) Detail of the 360–470 nm range for the samples' reflectance.
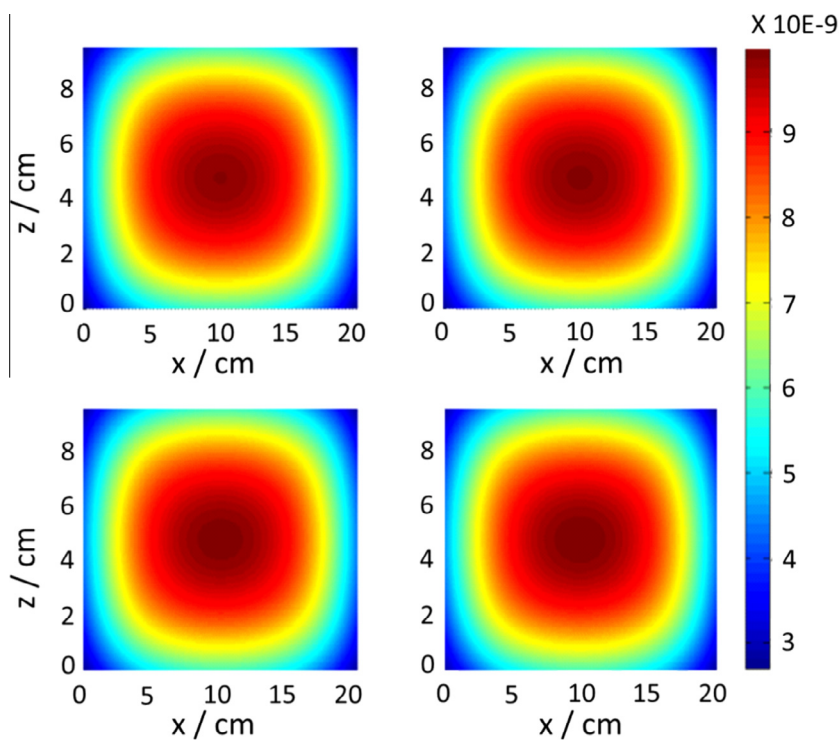

Fig. 5. Local superficial rate of photon absorption (Einstein cm^{-2} s^{-1}) under UV irradiation. Upper row: Ti and 0.025CeTi. Lower row: 0.05CeTi and 0.25CeTi.
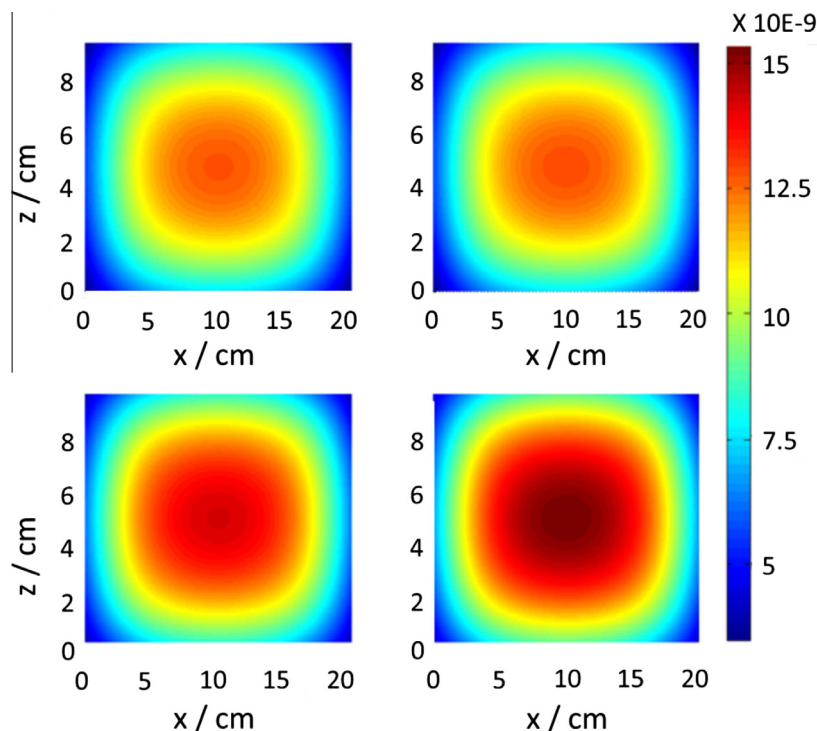
Fig. 6. Local rate of photon absorption (Einsten $cm^{-2} s^{-1}$) under Visible irradiation. Upper row: Ti and 0.025CeTi. Lower row: 0.05CeTi and 0.25CeTi.

Table 2
Sample chemical composition and morphological properties.

Sample	Ce/Ti TXRF	BET surface area ($m^2 g^{-1}$)	Porosity (%)	Anatase size (nm)	Fluorite size (nm)[a]
Ti	–	113.5	47.9	12.1	–
0.025CeTi	0.03	78.0	35.7	13.2	–
0.05CeTi	0.06	75.5	34.4	15.0	5.3
0.25CeTi	0.30	108.8	42.6	15.2	8.5

[a] Determined from synchrotron X-ray Diffraction [13].

CeO$_2$ references, respectively. Note that we did not detect the fluorite phase for samples with a CeO$_2$ content equal or above the one of the 0.05CeTi specimen. The structural characteristics of the samples were further characterized with the help of Raman spectroscopy (Fig. 8). The TiO$_2$ reference shows major Raman bands

ascribable to the TiO$_2$ anatase at 144, 195, 399, 517, and 639 cm^{-1} [37,38]. The pure cubic CeO$_2$ shows a typical single Raman band at 465 cm^{-1} [39,40]. Similar to the XRD results, composite samples always display the presence of the anatase phase but fluorite is only detected for samples with a CeO$_2$ content equal or above the 0.05CeTi specimen. Figs. 7 and 8 also display the evolution of the samples under reaction conditions. According to both XRD and Raman, the anatase TiO$_2$ and fluorite CeO$_2$ main phases do not suffer significant modifications.

Table 3 displays the band gap of samples assuming an indirect gap semiconductor indicating a typical continuous increase of absorption in the visible region of the band gap within experimental error (ca. 0.03 eV) with the mol% of CeO$_2$ of the material. Table 3 also presents the band gap of the samples after reaction. No important modification of the band gap energy was detected with respect to fresh samples.
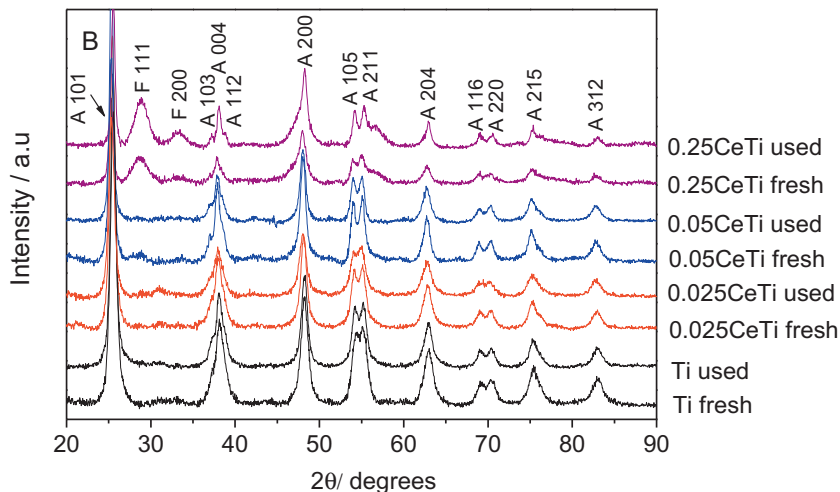

Fig. 7. XRD spectra for Ti reference and *x*CeTi composite samples. Fresh and spent (used under UV conditions) spectra are presented for each sample. XRD peaks (A: Anatase TiO$_2$, F: Fluorite CeO$_2$).
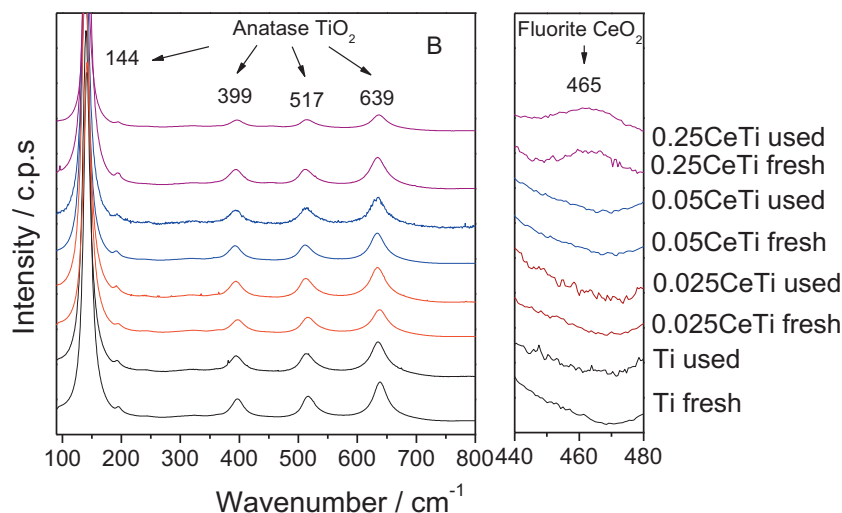
Fig. 8. Raman spectra for Ti reference and *x*CeTi composite samples. Fresh and spent (used under UV conditions) spectra are presented for each sample.

Table 3
Band gaps of the samples.

	Fresh band gap (eV)	Used band gap (eV)
Ti	3.02	3.02
0.025CeTi	2.97	2.96
0.05CeTi	2.53	2.54
0.25CeTi	2.50	2.50

4.2. Degradation of acetaldehyde: photocatalytic reaction rates

Under conditions detailed in Section 2.3, the average (surface-normalized) reaction rate can be obtained using Eq. (12) where Q is the volumetric flow rate of the stream fed, $\langle C_{Ac} \rangle_{in}$ and $\langle C_{Ac} \rangle_{out}$ are the averaged acetaldehyde concentrations of the inlet and outlet streams of the reactor, respectively, A_{BET} is the BET surface area and m is the mass of catalyst as a thin-layer coating on the borosilicate plate.

$$\langle r_{Ac} \rangle = \frac{Q(\langle C_{Ac} \rangle_{in} - \langle C_{Ac} \rangle_{out})}{A_{BET} \, m} \qquad (12)$$

The rate of acetaldehyde photo-degradation for the samples is presented in Fig. 9(A) and (B). Acetaldehyde was not degraded in the absence of illumination indicating that there was no dark reaction at the surface of samples. The maximum reaction rate is obtained for 0.025CeTi/0.05CeTi for UV/Visible photo-oxidation, respectively. These values correspond to an enhancement factor of 2.1/3.8 with respect to the TiO$_2$ reference photo-catalyst, respectively. We note that, in previous works concerning toluene photo-elimination, the TiO$_2$ catalyst here used was shown to be more active than the well-known Evonik P25 reference (previously called Degussa P25) [14,41], providing thus a proof of the outstanding degradation activity obtained with the CeO$_2$–TiO$_2$ samples. Interesting to stress is that the enhancement of the activity with respect to nano-anatase concerns both UV and visible light, indicating the suitability of low CeO$_2$-content composite materials for the use of sunlight as a green, renewable energy source of the degradation reaction. It can be also mentioned that, in previous reports concerning toluene degradation [13,14,26], the maximum photocatalytic activity under UV and visible light was detected for the same samples containing 2.5 mol% and 5 mol% of CeO$_2$, respectively. This also agrees with previous literature reports, where maximum activity is observed at ceria contents below 10 mol% [6,8].
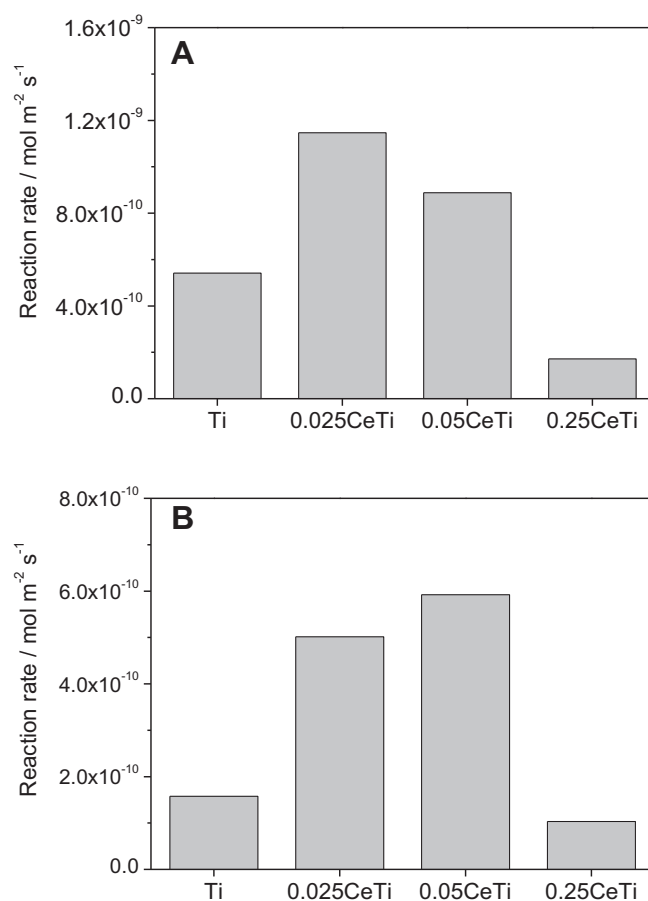

Fig. 9. Reaction rate normalized per surface area for Ti reference and *x*CeTi composite samples. (A) Under UV irradiation. (B) Under visible irradiation.

4.3. Radiation incidence and absorption efficiency

The radiation incidence efficiency (η_I) depends directly of both the reactor configuration and the system optical properties, and can be defined by Eq. (13). This parameter is helpful for comparing different configurations of photoreactors. Very high incidence efficiency can be obtained with annular reactors having a lamp placed at the central axis of the system [29]. Complementary optical

Table 4
Radiation absorption efficiency for samples and lamps.

	Ti	0.025CeTi	0.05CeTi	0.25CeTi
η_A UV (%)	88.3	88.3	88.9	89.1
η_A VIS (%)	39.0	39.2	43.4	46.7

devices, like reflecting mirrors, permit to increase this parameter. In our case the radiation incidence efficiency for both lamps is 13.5%.

$$\eta_I = \frac{\int_A \int_\lambda q_\lambda d\lambda dA}{\sum_{L=1}^{L=7} \int_\lambda P_{\lambda,L} d\lambda} \times 100 \tag{13}$$

The radiation absorption efficiency (η_A) relates to Superficial Rate of Photon Absorption with the incident radiation flow at the catalytic film (Eq. (14)). The $e^{a,s}$ displays, as it has been mentioned, a strong spectral dependence and allows quantitative comparisons concerning different light sources and samples.

$$\eta_A = \frac{\int_A \int_\lambda e_\lambda^{a,s} d\lambda dA}{\int_A \int_\lambda q_\lambda d\lambda dA} \times 100 \tag{14}$$

The obtained values for the parameter defined in Eq. (14) and the cases of the UV and visible lamps and all samples here studied are summarized in Table 4. The high values of absorbance and the small $e^{a,s}$ differences between the samples in the UV spectral range lead always to high radiation absorption efficiencies; in all cases above 88%. A different result has been obtained under visible irradiation condition. A continuous increase of $\langle e^{a,s}\rangle_A$ values ($8.53 \times 10^{-9}/8.58 \times 10^{-9}/9.51 \times 10^{-9}/1.02 \times 10^{-8}$ Einstein cm^{-2} s^{-1}) is related to an increasing CeO$_2$ loading (Ti/0.025CeTi/0.05CeTi/0.25CeTi) in the samples. This enhancement of light absorption affects positively the radiation absorption efficiency, which grows for all samples with respect to the titania reference. As described in the introduction section, this is an expected result due to the addition of ceria, a visible light absorber semiconductor, albeit Table 4 provides a quantitative measurement concerning sample differences.

It is obvious that (η_I) and (η_A) do not give information about the photocatalytic activity of the samples because are independent of the reaction and the operating conditions. However, we must recall that the last condition holds for (η_A) as long as the reactive medium is optically inactive in the useful region of the lamp emission spectrum (e.g. independent of flow rate of contaminated air, in our case, the acetaldehyde concentration) [29]. Concluding, these two parameters are useful to compare the potential of the reaction systems and samples in relation to the efficient use of light.

4.4. Quantum and photonic efficiencies

The reaction efficiencies under UV and Visible lights can be determined from the reaction rate and: (i) the Superficial Rate of Photon Absorption for the quantum (or true) efficiency (η_q; and
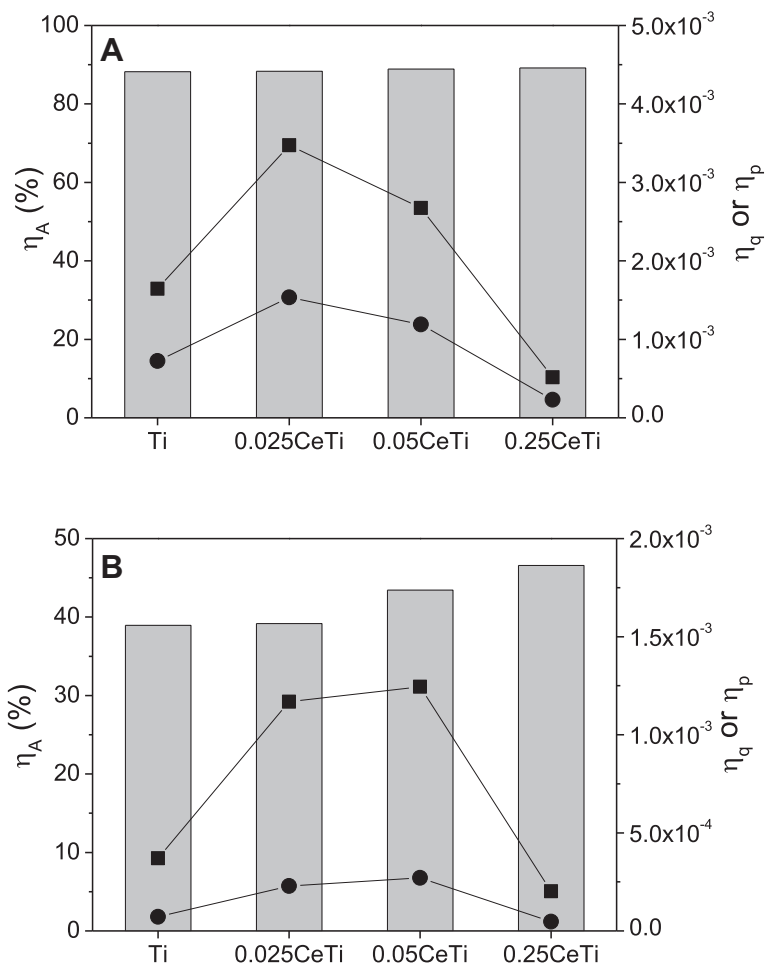

Fig. 10. Radiation absorption efficiency (Bar); quantum efficiency (square) and photonic efficiency (circle) for Ti reference and *x*CeTi composite samples. (A) Under UV irradiation. (B) Under visible irradiation.

(ii) the net radiation flux on the catalytic film for the photonic (or apparent) efficiency (η_p), according to Eqs. (15) and (16) respectively.

$$\eta_q = \frac{\langle r \rangle_A}{\langle e^{a,s} \rangle_A} \times 100 \tag{15}$$

$$\eta_p = \frac{\langle r \rangle_A}{\langle q \rangle_A} \times 100 \tag{16}$$

Fig. 10(A) and (B) show the quantum efficiency and photonic efficiency for the samples 0.025CeTi, 0.05CeTi, 0.25CeTi and the Ti reference under UV and Visible irradiation, respectively.

The first point to note is the relative low (quantum or photonic) efficiencies displayed by the materials albeit their relatively good absorption capabilities (Table 4). Values below 0.005 are always obtained in Fig. 10. Such a low magnitude values point out that recombination losses are rather significant. It should be noted that, in any case, the best values reported in Figs. 9 and 10 for CeO$_2$–TiO$_2$ composites are significantly higher than those of the nano-titania reference system by factors exceeding 2 for both UV and visible light excitation. The literature discusses the absolute value of the quantum efficiency of titania-based photocatalysts without having a clear conclusion; nevertheless they are usually below 1% [42]. We can stress also that gas phase reactions (this work and Refs. [29,42]) would show lower values than liquid phase ones [30,32,42,43]. However the absence of normalization in considering, for example, the real surface area of the catalyst accessible to light, as well as details of the computational procedures used to calculate the number of photons effectively reaching the sample surface, do not allow to provide a general discussion of this point.

Comparison of Figs. 9 and 10 also highlights several additional points. The first one is related to the fact that, when comparing quantum efficiencies, the Ce–Ti molar ratio between 0.025 and 0.05 provides maximum performance irrespective of the illumination conditions. Under UV and Visible illumination such maximum corresponds to the 0.025CeTi and 0.05CeTi samples, respectively. The close proximity of the maximum, as well as the high activity of the 0.025CeTi samples in all conditions tested, indicate that photo-physical events would govern the acetaldehyde photo-oxidation. The 0.025CeTi would be the sample with the lower charge carrier recombination rate. However, the optimum achieved under visible illumination with the 0.05CeTi sample would additionally indicate that the optical properties also contribute, although to a modest extent, to the photo-activity. This can be observed in Fig. 10B where η_A increases for higher Ce content.

Finally, it should be noted that the ratio between quantum and photonic efficiencies of each sample provides a roughly constant value (within 2% variation) for the UV case but not for the visible one. Fig. 11 illustrates this point; the use of a normalized ratio between these two quantities makes obvious this issue. Note that such point is relatively easily to predict if considered that such ratio is inversely proportional to the η_A coefficient included in Table 4. In spite of this, the plot in Fig. 11 indicates that the use of photonic efficiencies is, as expected, only reasonably accurate as long as the photo-physical properties of the photocatalysts do not differ markedly.

5. Conclusions

Degradation of acetaldehyde using CeO$_2$–TiO$_2$ composite materials was investigated under UV and visible light illumination conditions. Efficiency parameters were obtained in order to quantitatively compare the performance of the catalysts. To this end, the emission properties of the lamps were evaluated and modeled with a reasonable accuracy (7% and 10% for UV and visible lamp respectively). Also, the local superficial rate of photon absorption at each point of the sample surface was calculated using transmittance and reflectance optical data obtained for each composite and reference samples. The CeO$_2$–TiO$_2$ composite materials exhibit similar light absorption capabilities among them and with respect to the titania reference in the UV region while an increasing absorption trend with the CeO$_2$ content of the material is observed for the visible region. This was quantitatively estimated trough the radiation absorption efficiency.

The quantum efficiency parameter reaches a single maximum within the CeO$_2$–TiO$_2$ composite sample series. This maximum corresponds to the 0.025CeTi sample under UV irradiation and to the 0.05CeTi sample under visible irradiation, which outperforms the titania reference material by a factor larger than 2 in all illumination conditions. This demonstrates the potential of the material for the degradation of the tested pollutant. The behavior of the CeO$_2$–TiO$_2$ samples under different illumination conditions would suggest that photo-physical events are of significant importance in control the photo-chemical activity of the system.

Appendix A.

The integration limits can be obtained using the following equations:

$$\varphi_{min} = \tan^{-1}\left(\frac{X_L - Xs}{Y_L}\right) - \sin^{-1}\left(\frac{R_L}{(X_L - Xs)^2 + (Y_L)^2}\right)$$

$$\varphi_{max} = \tan^{-1}\left(\frac{X_L - Xs}{Y_L}\right) + \sin^{-1}\left(\frac{R_L}{(X_L - Xs)^2 + (Y_L)^2}\right)$$
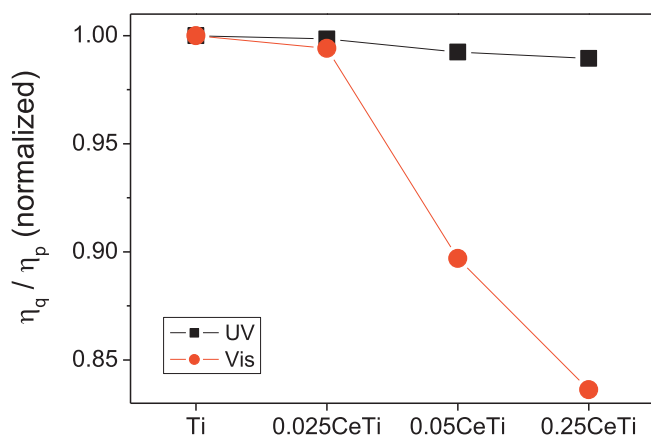

Fig. 11. Ratio between the quantum efficiency and photonic efficiency for Ti reference and xCeTi composite samples. Data is normalized to provide an unitary ratio for the Ti reference sample.

$$\theta_{\min}(\varphi) = \cos^{-1} \frac{-Zs}{(X_{\mathrm{Lm}}(\varphi) - Xs)^2 + Y_{\mathrm{Lm}}(\varphi)^2 + Zs^2}$$

$$\theta_{\max}(\varphi) = \cos^{-1} \frac{Z_L - Zs}{(X_{\mathrm{Lm}}(\varphi) - Xs)^2 + Y_{\mathrm{Lm}}(\varphi)^2 + Zs^2}$$

where:

$$X_{\mathrm{Lm}}(\varphi) = X_L + (Xs - Y_L)\cos\varphi^2 + (Y_L)(\cos\varphi\ \mathrm{sen}\ \varphi)$$
$$- \mathrm{sen}\ \varphi \sqrt{(R_L^2 - (Y_L\ \mathrm{sen}\varphi + (Xs - X_L)\cos\varphi)^2)}$$

$$Y_{\mathrm{Lm}}(\varphi) = (Y_L)\cos\varphi^2 - (Xs - X_L)(\cos\varphi\ \mathrm{sen}\varphi)$$
$$- \cos\varphi \sqrt{(R_L^2 - (Y_L\ \mathrm{sen}\ \varphi + (Xs - X_L)\cos\varphi)^2)}$$

where: X_L, Y_L and Z_L, are the coordinates of the points located on the surface of the lamp. Xs, Ys and Zs are the coordinates of the points located on the surface of the films.

Appendix B. Supplementary data

Supplementary data associated with this article can be found, in the online version, at http://dx.doi.org/10.1016/j.cej.2014.06.056.

References

[1] M.R. Hoffman, S.T. Martin, W. Choi, D.W. Bahneman, Environmental applications of semiconductor photocatalysis, Chem. Rev. 95 (1995) 69–121.

[2] O. Carp, C.L. Huisan, A. Reller, Photoinduced reactivity of titanium dioxide, Prog. Solid State Chem. 32 (2004) 33–145.

[3] H. Thu, M. Karkmaz, E. Puzenat, C. Guillard, J.M. Herrmann, From the fundamentals of photocatalysis to its applications in environment protection and in solar purification of water in arid countries, Res. Chem. Intermediat. 31 (2005) 449–461.

[4] A. Kubacka, G. Colón, M. Fernández-García, Advanced nanoarchitectures for solar photocatalytic applications, Chem. Rev. 112 (2012) 1555–1614.

[5] S. Parasupree, Y. Suzuki, S. Prisa-Art, S. Yoshikawa, Preparation and characterization of mesoporous TiO$_2$–CeO$_2$ nanopowders respond to visible wavelength, J. Solid State Chem. 178 (2005) 128–134.

[6] G. Li, D. Zhang, Y.C. Yu, Thermally stable ordered mesoporous CeO$_2$/TiO$_2$ visible-light photocatalysts, Phys. Chem. Chem. Phys. 11 (2009) 3775–3782.

[7] V. Štengl, S. Bakardejieva, N. Murafa, Preparation and photocatalytic activity of rare earth doped TiO$_2$ nanoparticles, Mater. Chem. Phys. 114 (2009) 217–226.

[8] H. Lin, M. Wang, Y. Wang, Y. Liang, W. Cao, Y. Su, Ionic liquid-templated synthesis of mesoporous CeO$_2$–TiO$_2$ nanoparticles and their enhanced photocatalytic activities under UV or visible light, J. Photochem. Photobiol. A 223 (2011) 157–162.

[9] Y. Wang, B. Li, C. Zhang, L. Cui, S. Kang, X. Li, L. Zhou, Ordered mesoporous CeO$_2$–TiO$_2$ composites: highly efficient photocatalysts for the reduction of CO$_2$ with H$_2$O under simulated solar irradiation, Appl. Catal. B 130–131 (2013) 277–284.

[10] Y. Liu, P. Fang, Y. Cheng, Y. Gao, F. Chen, Z. Liu, Y. Dai, Study on enhanced photocatalytic performance of cerium doped TiO$_2$-based nanosheets, Chem. Eng. J. 219 (2013) 478–485.

[11] C. Karunakaran, P. Gomathisankar, Solvothermal synthesis of CeO$_2$–TiO$_2$ nanocomposite for visible light photocatalytic detoxification of cyanide, ACS Sus. Chem. Eng. 1 (2013) 1555–1563.

[12] J. Santiago-Morales, A. Aguera, M.M. Gómez, A.R. Fernández-Alba, J. Gimeno, S. Esplugas, R. Rosal, Transformation products and reaction kinetics in simulated solar light photocatalytic degradation of propranolol using Ce-doped TiO$_2$, Appl. Catal. B 129 (2013) 13–29.

[13] M.J. Muñoz-Batista, M.N. Gómez-Cerezo, A. Kubacka, D. Tudela, M. Fernández-García, Role of interface contact in CeO$_2$–TiO$_2$ photocatalytic composite materials, ACS Catal. 4 (2014) 63–72.

[14] M.J. Muñoz-Batista, M. Ferrer, M. Fernández-García, A. Kubacka, Abatement of organics and Escherichia coli using CeO$_2$–TiO$_2$ composite oxides: ultraviolet and visible light performances, Appl. Catal. B 154–155 (2014) 350–359.

[15] M.D. Hernández-Alonso, A.B. Hungría, A. Martínez-Arias, M. Fernández-García, J.M. Coronado, J.C. Conesa, J. Soria, EPR study of the photoassisted formation of radicals on CeO$_2$ nanoparticles employed for toluene photooxidation, Appl. Catal. B 50 (2004) 167–175.

[16] P. Ji, J. Zhang, F. Chen, M. Anpo, Study of adsorption and degradation of acid orange 7 on the surface of CeO$_2$ under visible light irradiation, Appl. Catal. B 85 (2009) 148–154.

[17] G. Chen, J. Xiong, F.J. Stadler, A facile polyol-mediated approach to tunable CeO2 microcrystals and their photocatalytic activity, Powder Technol. 249 (2013) 89–94.

[18] Y. Wang, F. Wang, Y. Chen, D. Zhang, B. Li, S. Kang, X. Li, L. Cui, Enhanced photocatalytic performance of ordered mesoporous Fe-doped CeO$_2$ catalysts for the reduction of CO$_2$ with H$_2$O under simulated solar irradiation, Appl. Catal. B 147 (2014) 602–609.

[19] G.E. Imoberdorf, A.E. Cassano, O.M. Alfano, H.A. Irazoqui, Modeling of a multiannular photocatalytic reactor for perchloroethylene degradation in air, AIChE J. 52 (2006) 1814–1823.

[20] L. Zhang, W.A. Anderson, A finite model for the prediction of the UV radiation field around a linear lamp, Chem. Eng. J. 65 (2010) 1513–1521.

[21] M.M. Ballari, M. Hunger, G. Hüsken, H.J.H. Brouwers, Modelling and experimental study of the NOx photocatalytic degradation employing concrete pavement with titanium dioxide, Catal. Today 151 (2010) 71–76.

[22] Q.L. Yu, M.M. Ballari, H.J.H. Brouwers, Indoor air purification using heterogeneous photocatalytic oxidation. Part II: kinetic study, Appl. Catal. B 99 (2010) 58–65.

[23] A.L.L. Zazueta, H. Destallaits, G.L. Puma, Radiation field modeling and optimization of a compact and modular multi-plate photocatalytic reactor (MPPR) for air/water purification by Monte Carlo method, Chem. Eng. J. 217 (2013) 475–485.

[24] C. Passalía, O.M. Alfano, R.J. Brandi, Modeling and experimental verification of a corrugated plate photocatalytic reactor using computational fluid dynamics, Ind. Eng. Chem. Res. 50 (2011) 9077–9086.

[25] G.E. Imoberdorf, H.A. Irazoqui, A.E. Cassano, O.M. Alfano, Photocatalytic degradation of tetrachloroethylene in gas phase on TiO$_2$ films: a kinetic study, Ind. Eng. Chem. Res. 44 (2005) 6075–6085.

[26] M.J. Muñoz-Batista, A. Kubacka, M.N. Gómez-Cerezo, D. Tudela, M. Fernández-García, Sunlight-driven toluene photo-elimination using CeO$_2$–TiO$_2$ composite systems: a kinetic study, Appl. Catal. B 140–141 (2013) 626–635.

[27] M.L. Sauer, D.F. Ollis, Photocatalyzed oxidation of ethanol and acetaldehyde in humidified air, J. Catal. 158 (1996) 570–582.

[28] L. Zhang, W.A. Anderson, Kinetic analysis of the photochemical decomposition of gas-phase chlorobenzene in a UV reactor: quantum yield and photonic efficiency, Chem. Eng. J. 218 (2013) 247–252.

[29] G.E. Imoberdorf, A.E. Cassano, H.A. Irazoqui, O.M. Alfano, Simulation of a multi-annular photocatalytic reactor for degradation of perchloroethylene in air: parametric analysis of radiative energy efficiencies, Chem. Eng. Sci. 64 (2007) 1138–1154.

[30] M.L. Satuf, R.J. Brandi, A.E. Cassano, O.M. Alfano, Quantum efficiencies of 4-chlorophenol photocatalytic degradation and mineralization in a well-mixed slurry reactor, Ind. Eng. Chem. Res. 46 (2007) 43–51.

[31] J. Marugan, D. Hufschmidt, M.-J. López-Muñoz, V. Selzer, D. Bahnemann, Photonic efficiency for methanol photooxidation and hydroxyl radical generation on silica-supported TiO$_2$ photocatalysts, Appl. Catal. B 62 (2006) 201–207.

[32] M.B. Marcó, A.d.L. Quiberonia, A.C. Negro, J.A. Reinheimer, O.M. Alfano, Evaluation of the photocatalytic inactivation efficiency of dairy bacteriophages, Chem. Eng. J. 172 (2011) 987–993.

[33] P.G. De Gennes, C. Taupin, Microemulsions and the flexibility of oil/water interfaces, J. Phys. Chem. 86 (1982) 2294–2303.

[34] M. Fernández-García, X. Wang, C. Belver, J.C. Hanson, J.A. Rodriguez, Anatase–TiO$_2$ nanomaterials: morphological/size dependence of the crystallization and phase behavior phenomena, J. Phys. Chem. C 111 (2007) 674–682.

[35] A.E. Cassano, C.A. Martin, R.J. Brandi, O.M. Alfano, Photoreactor analysis and design: fundamentals and applications, Ind. Eng. Chem. Res. 34 (1995) 2155–2201.

[36] D.K. Edwards, Solar absorption by each element in an absorber-coverglass array, Solar Energy 19 (1977) 401–402.

[37] M. Fernández-García, A. Martínez-Arias, A. Fuerte, J.C. Conesa, Nanostructured Ti−W mixed-metal oxides: structural and electronic properties, J. Phys. Chem. B 109 (2005) 6075–6083.

[38] M. Mikami, S. Nakamura, O. Kitao, H. Arakawa, Lattice dynamics and dielectric properties of TiO$_2$ anatase: a first-principles study, Phys. Rev. B 66 (2002) 155213–155216.

[39] J. Fang, X. Bi, D. Si, Z. Jiang, W. Huang, Spectroscopic studies of interfacial structures of CeO$_2$–TiO$_2$ mixed oxides, Appl. Surf. Sci. 253 (2007) 8952–8961.

[40] K. Nagaveni, M.S. Hegde, G. Madras, Structure and photocatalytic activity of Ti$_{1−x}$M$_x$O$_{2±\delta}$ (M = W, V, Ce, Zr, Fe, and Cu) synthesized by solution combustion method, J. Phys. Chem. B 108 (2004) 20204–20212.

[41] A. Kubacka, M. Fernández-García, G. Colón, Nanostructured Ti–M mixed-metal oxides: toward a visible light-driven photocatalyst, J. Catal. 254 (2008) 272–284.

[42] M. Peláez, N.T. Nolan, S.C. Pillai, M.K. Severy, P. Falaras, A.G. Kontos, P.S.M. Dunlop, J.A. Bryne, D.D. Dionysiou, A review on the visible light active titanium dioxide photocatalysts for environmental applications, Appl. Catal. B 125 (2012) 331–358.

[43] A. Manassero, M.C. Satuf, O.M. Alfano, Evaluation of UV and visible light activity of TiO$_2$ catalysts for water remediation, Chem. Eng. J. 225 (2013) 378–386.